ARTICLES

Femtosecond Real-Time Probing of Reactions. 12. Vectorial Dynamics of Transition States

T. Baumert,† S. Pedersen, and A. H. Zewail*

Arthur Amos Noyes Laboratory of Chemical Physics,‡ California Institute of Technology, Pasadena, California 91125

Received: September 9, 1993®

Femtosecond time-resolved techniques with KETOF (kinetic energy time-of-flight) detection in a molecular beam are developed for studies of the vectorial dynamics of transition states. Application to the dissociation reaction of IHgI is presented. For this system, the complex $[I\cdots Hg\cdots I]^{\ddagger *}$ is unstable and, through the symmetric and asymmetric stretch motions, yields different product fragments: $[I\cdots Hg\cdots I]^{\ddagger *} \rightarrow HgI(X^2\Sigma^+) + I(^2P_{3/2})$ [or $I^*(^2P_{1/2})$] (1a); $[I\cdots Hg\cdots I]^{\ddagger *} \rightarrow Hg(^1S_0) + I(^2P_{3/2}) + I(^2P_{3/2})$ [or $I^*(^2P_{1/2})$] (1b). These two channels, (1a) and (1b), lead to different kinetic energy distributions in the products. It is shown that the motion of the wave packet in the transition-state region can be observed by MPI mass detection; the transient time ranges from 120 to 300 fs depending on the available energy. With polarized pulses, the vectorial properties (transition moments alignment relative to recoil direction) are studied for fragment separations on the femtosecond time scale. The results indicate the nature of the structure (symmetry properties) and the correlation to final products. For 311-nm excitation, no evidence of crossing between the I and I* potentials is found at the internuclear separations studied. (Results for 287-nm excitation are also presented.) Molecular dynamics simulations and studies by laser-induced fluorescence support these findings.

I. Introduction

With polarized femtosecond excitation and analyzed femtosecond detection, using laser-induced fluorescence (LIF) or multiphoton ionization mass spectrometry (MPI-MS), one gains the ability to examine the vectorial properties of molecular dynamics in real time.[1,2] For nonreactive systems, the change in the time-dependent alignment gives the molecular structure.[3,4] For reactive systems, it provides new information on the evolution[1,2,5-7] of the angular momenta and the anisotropic decay of the fragment orientation.

In this paper, in the series, we develop kinetic energy time-of-flight (KETOF) as a method for obtaining the vectorial properties of transition states on the femtosecond time scale. As with time-of-flight photofragment translation spectroscopy, we examine the polarization properties (see Appendix for original references and also refs 8–10 for reviews) of the velocity distribution anisotropy, but now at femtosecond resolution of the dynamics. The mass selectivity enables the separate observation of parent and fragment dynamics. In general, ionization of the initial parent is not observed in the mass spectrum if the reaction time is ultrashort and competition of dissociation with ionization is efficient. This problem is circumvented by femtosecond pulses as the system can be "frozen out" prior to fragmentation, and the ladder switching[11] to product ionization at long times can be controlled. Examples can be found in the studies of elementary reactions (e.g., Na_2,[12] CH_3I,[13] and OClO[14]) and of clusters (e.g., Na_n[15] and $(NH_3)_n$[16]). A single-pulse femtosecond experiment on a molecular beam with KETOF detection, studying MPI-induced fragmentation processes in Na_2,[17] was reported, but no femtosecond time-resolved KETOF experiments have been reported up to now.

The application made here of the femtosecond/KETOF method involves a study of the dissociation reaction of IHgI:

$$IHgI + h\nu \rightarrow [I\cdots Hg\cdots I]^{\ddagger *} \rightarrow HgI(X^2\Sigma^+) + I(^2P_{3/2}) \quad (2a)$$

For this product channel the wave packet motion ultimately involves the asymmetric stretch mode of the complex. Both products are in their ground state. Energetically, at the wavelengths used, the iodine atoms can also be formed in the excited state

$$IHgI + h\nu \rightarrow [I\cdots Hg\cdots I]^{\ddagger *} \rightarrow HgI(X^2\Sigma^+) + I^*(^2P_{1/2}) \quad (2b)$$

and this channel also involves the asymmetric stretch motion. The two surfaces leading to the I and I* asymptotes are separated by the spin–orbit splitting of free iodine atoms (7600 cm^{-1}) at long internuclear distances; the splitting is less at the complex geometry near the Franck–Condon region, as discussed below. One important question addressed here is the nature of the two surfaces and the crossing (or lack thereof) between them.

If the complex is prepared above the limit of total dissociation, then it is possible to produce the three atomic fragments:

$$IHgI + h\nu \rightarrow [I\cdots Hg\cdots I]^{\ddagger *} \rightarrow I(^2P_{3/2}) + Hg(^1S_0) + I(^2P_{3/2}) \quad (2c)$$

The nuclear motions in this case involve the symmetric stretch mode.

In these channels described above the fragment atom (or diatom) has a different kinetic energy in each case, and resolution of the kinetic energy in the velocity distribution anisotropy gives the vectorial correlation corresponding to the channel of interest. The scalar part (kinetic energy release) of the dissociation is studied here with the transient time measured as the wave packet leaves the transition-state region of the complex. The vectorial part (transition moment correlation with fragmentation) of the dissociation process is examined by the change in the velocity distributions at times between 0 and 500 fs. The approach adds a useful dimension to femtosecond transition-state spectroscopy (FTS) and may be applied to the different detection schemes of

† Deutsche Forschungsgemeinschaft (DFG) postdoctoral fellow.
‡ Contribution No. 8847.
* Abstract published in *Advance ACS Abstracts*, November 1, 1993.

0022-3654/93/2097-12447$04.00/0

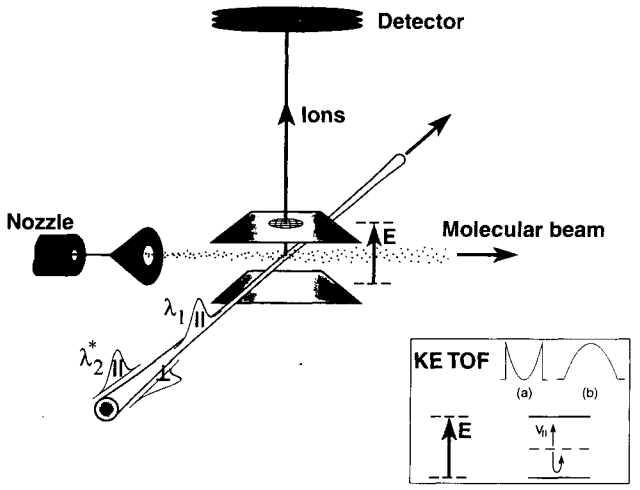

Figure 1. Schematic of the experimental approach utilizing two polarized femtosecond pulses and a TOF mass spectrometer. The femtosecond lasers, the molecular beam, and the TOF axis are mutually perpendicular. The TOF axis is defined by the electric field **E**. For the experiments described here, the pump laser (λ_1) polarization was kept parallel to the TOF axis, whereas the probe laser (λ_2*) polarization was either parallel or perpendicular with respect to the pump. On the left (a) a distribution resulting from a pure parallel transition is indicated, whereas the distribution to the right (b) resembles a pure perpendicular transition (see text), if the pump laser polarization is parallel to the TOF axis.

LIF,[2] absorption,[18] MPI-TOF,[12,13,16] photoelectron detection[15] using ZEKE photoelectron spectroscopy,[19] and stimulated emission pumping.[20]

The outline of the paper is as follows: In section II, a discussion of the approach is given. The experimental description is given in section III, followed by the results in section IV. The discussion in section V focuses on the femtosecond dynamics and the reaction path, with reference to other findings from molecular dynamics and laser-induced fluorescence studies. The conclusions are given in section VI, followed by an Appendix detailing anisotropy and rotational alignment in pump–probe experiments.

II. Femtosecond/KETOF Method

In the studies of reaction dynamics on the femtosecond time scale, the two attributes of TOF,[21] the mass selectivity and the possibility of measuring fragment energies, add a unique dimension. Not only can the decay of the parent complex be monitored directly, but also the delay of the fragments. By measuring the temporal evolution of fragments with different kinetic energy, different fragmentation channels leading to the same fragment can, in principle, be distinguished. As the TOF axis is well-defined, rotating the pump laser polarization, with respect to the TOF axis, and analyzing the resulting KETOF spectra gives the vectorial properties, such as the alignment of a transition moment with respect to the excitation polarization. Rotating the probe laser polarization with respect to the pump laser polarization can then finally deliver information on the alignment of the fragment transition moment in a particular dissociation process. In the following, we will briefly describe the basic idea and relate its application to the case under study.

In this application of a TOF spectrometer, ions are created by MPI with femtosecond laser pulses. The interaction region is in the electric field of a parallel plate capacitor with a ringlike aperture in the direction of the detector; the aperture is covered with a mesh in order to ensure a homogeneous electric field in the interaction region. The direction of this electric field thus defines our TOF axis (Figure 1). After leaving this extraction region, the ions are further accelerated and are detected with a set of multichannel plates after they have passed the field-free drift region. Solving the classical equations of motion yields the result that the flight time T (for all three regions) is proportional to the square root of the mass m of the ionized particles.[21]

In terms of mass resolution, a well-defined initial spatial position and a well-defined time zero for creating the ions is important. The starting spatial distribution is determined by the diameter of the focused laser beam (on the order of 50–100 μm), whereas the starting time is determined by the time duration of the laser pulse. Using femtosecond laser pulses, and femtosecond or picosecond pump–probe delay times, the TOF broadening due to poorly defined starting times is negligible, as the flight time is on the order of microseconds. The mass resolution of our TOF spectrometer is about 1:150.

The velocity distribution due to fragmentation causes a spread around the central time-of-flight, T. The spread in the time-of-flight for the ionized fragments is a linear function of their velocity projection, $v_{\|}$, onto the TOF axis (see below). Consider two identical ions formed at the same initial position $\mathbf{r}_1$ with equal but oppositely directed velocities ($\pm v_{\|}$) along the TOF axis (ion 1 travels up). Ion 2 is decelerated by the electric field **E** of the extraction region, stopping at a position $\mathbf{r}_2$ directly below $\mathbf{r}_1$. It is then accelerated, returning to $\mathbf{r}_1$ with its original speed, in the same time it took to decelerate to $\mathbf{r}_2$. Subsequently, the motion of ion 2 is identical to that of ion 1, which it now continues to lag by the "turn-around" time. Hence, t, the position relative to the central time T in the TOF spectrum corresponding to $v_{\|}$ is given by (from $F = ma = q\mathbf{E}$)

$$t = -(mv_{\|}/q\mathbf{E}) \tag{3}$$

The total time-of-flight, $T + t$, is a linear function of the velocity projection, $v_{\|}$. For a fixed translational energy release (recoil speed v_0) the maximum time spread for a fragment ion becomes

$$\Delta t = 2(mv_0/q\mathbf{E}) \tag{4}$$

Therefore, the kinetic energy of the ion ($^1/_2mv_0^2$) can be written as

$$E_{\text{kin}} = q^2E^2(\Delta t)^2/8m \tag{5}$$

In the type of experiment considered, two fragments are formed in the dissociation of the pump excited molecule. Because of the excitation distribution, determined by the pump polarization and the direction of the transition moment, there is a distribution in t, as discussed below.

The total energy in the center-of-mass frame (CM) is conserved, implying that[22]

$$E_{\text{avl}} = E_{\text{int}}^{\text{P}} + h\nu_{\text{pu}} - D_0^0 = E_{\text{int}} + E_{\text{t}} \tag{6}$$

where E_{avl} is the energy available to be partitioned among internal and translational degrees of freedom of the recoiling fragments, $E_{\text{int}}^{\text{P}}$ is the thermal internal energy of the parent molecule, $h\nu_{\text{pu}}$ is the pump energy, D_0^0 is the dissociation energy from the ground-state parent to the ground-state fragments, E_{int} is the total internal excitation energy of the two fragments, and E_{t} is the CM translational energy. In the CM frame, the two fragments share the total available translational energy, which means that

$$E_{\text{kin1}} = \frac{m_2}{m_1}E_{\text{kin2}} = E_{\text{t}}\left[1 + \frac{m_1}{m_2}\right]^{-1} \tag{7}$$

Consider the probing of a *free* fragment. Due to the small photon momentum, the translational energy available to the ion and ejected electron is shared unequally in a manner similar to eq 7. If, for example, a 100 amu fragment is ionized, leaving 5000 cm^{-1} available as translational energy, then the change in the fragment velocity is <3 m s^{-1}, while the electron velocity is $\sim 5 \times 10^5$ m s^{-1}. As the neutral fragment velocity in the CM frame is typically of order 10^3 m s^{-1}, it is practically unaltered by probing to ionization. Hence, the translational energy, E_{t}, of the parent dissociation can be deduced from the velocity profiles of the probe ionized fragments.

In the transition state a probe transition moment, $\mu_2(t)$, may

be defined. The orientation of this transition moment depends on the anisotropic distribution created by the pump pulse as well as the subsequent evolution of the excited complex in the transition state. Using different orientations of the pump (ϵ_{pu}) and probe (ϵ_{pr}) polarizations with respect to the TOF axis, different velocity profiles result, each of which characterizes distinct features (correlations) of the anisotropic distribution in the transition state. From this, one may deduce the nature of the pump transition (parallel *vs* perpendicular) and of the probe transition in the evolution of the transition state. In addition, it is possible to calculate the translational energy release. In the Appendix, we discuss these issues with focus on the anisotropic fragment distribution involved in pump–probe experiments. The velocity profile for free fragment probing is parabolic, characterized by an effective anisotropy parameter, β_{eff} (eq A11), which may differ from the anisotropy parameter, β, associated with the pump alone process (eq A3).

For illustration, we consider a specific example (see Figure 12). Suppose the pump pulse excites molecules that dissociate fast with respect to rotation and the parent transition is parallel, *i.e.*, the transition moment is parallel to the internuclear axis. In this case, we have $\chi_0(t) = 0°$ (see Appendix) and the pump creates a $\cos^2\theta$, dumbbell-shaped distribution. For the case when, in the transition state, the transition moment for probing is aligned along the direction of the internuclear axis of the complex $\mu_2 \| \mathbf{r}(t)$ (the direction $\mathbf{r}(t)$ is along the final recoil direction for a nonrotating molecule), the situation is easy to picture. If the probe is parallel to the pump ($\epsilon_{pr} \| \epsilon_{pu}$), then the distribution created by the pump pulse will be enhanced, yielding a maximum probability for the probed fragments to recoil along the pump polarization direction: $\theta = 0°$ or 180°. If, on the other hand, the probe is perpendicular to the pump ($\epsilon_{pr} \perp \epsilon_{pu}$), then the distribution is greatly reduced in magnitude and also altered. Consider next a different process in which the parent transition is perpendicular (see Figure 12). Here $\chi_0(t) = 90°$ and the pump excitation yields a $\sin^2\theta$, toroidal angular distribution of the fragments. Let us suppose that the transition moment, μ_2, in the transition state is still along the fragment recoil direction. If the probe is now parallel to the pump, then few fragments will be ionized by the probe, while if the probe is perpendicular to the pump, the velocity distribution created by the pump will be enhanced and carried over to the ionized fragments (ion fragmentation is faster than rotation). These distributions which change in shape with polarization thus reflect the correlation and symmetry; they are discussed in the Appendix.

III. Experimental Section

The femtosecond laser apparatus has been described in detail previously[23] and is discussed only briefly here. Femtosecond pulses were generated from a colliding pulse mode-locked ring dye laser (CPM) and amplified by a Nd:YAG-pumped pulsed dye amplifier (PDA). The recompressed output pulses had an (unattenuated) energy of 0.2–0.3 mJ at a repetition rate of 20 Hz. The 311 nm (fwhm = 5 nm) pump wavelength was generated by frequency-doubling a part of the PDA output in a 0.2-mm-thick KDP crystal. The 287-nm pump was generated by frequency mixing part of the PDA output at 622 nm with a residual part of the Nd:YAG output at 532 nm in a 0.5-mm-thick KD*P crystal. For the probe MPI we used the remaining output of the PDA (622 nm, fwhm = 13 nm).

The pump and probe beams, with proper attenuation and parallel or perpendicular polarization, were delayed in time relative to one another in a Michelson interferometer and were then recombined collinearly and focused onto the IHgI molecular beam. Before entering the molecular beam, we routinely recorded autocorrelations of the probe (fwhm ~ 60 fs sech^2). Cross-correlations were derived by convoluting a Gaussian cross-correlation (100 fs) with the molecular response function of I_2 in a 622-nm excitation and 311-nm probe experiment, where the fluorescence at 340 nm was recorded as a function of the pump–probe delay time.[24]

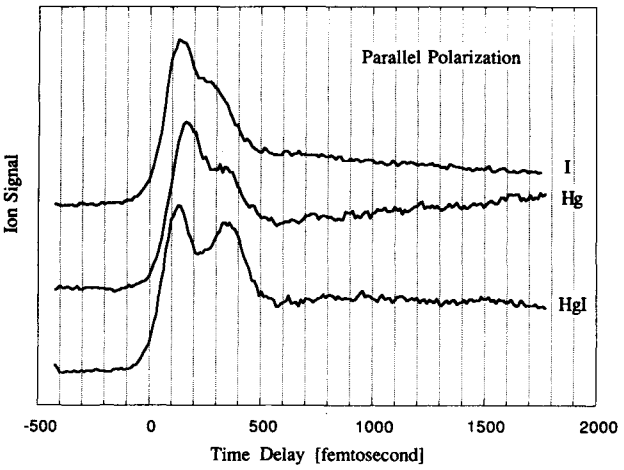

Figure 2. Femtosecond transients obtained by detecting the mass of HgI, Hg, and I for parallel laser polarization. Time zero is given with respect to half the rise of the parent IHgI.

The molecular beam consisted of an oven with a nozzle diameter of 0.3 mm. The oven was heated to 445 K (measured at the nozzle). MPI femtosecond experiments on the skimmed molecular beam were carried out in a differentially-pumped ionization chamber about 12 cm downstream from the nozzle. The TOF spectrometer was used either in its mass resolution mode or in its kinetic energy resolution mode. The molecular beam, the lasers, and the TOF detection axes were mutually perpendicular. For the set of experiments described here, the pump laser polarization was kept fixed and parallel to the TOF axis. A sketch of the experimental setup is shown in Figure 1.

The sample was 99.999% HgI_2 (Aldrich) containing the natural isotope distribution of Hg (196–204 amu). This resulted in a time-of-flight broadening on the HgI_2 parent and the HgI and Hg fragments. Therefore, the KETOF technique was applied to the iodine mass; for the other masses isotopically pure samples are needed.

Two types of data collection were used: For the transients, a boxcar gate was set to the mass under investigation, and the (femtosecond) delay line was scanned until a satisfactory signal-to-noise level on the transients was achieved. The KETOF transients on the fragment iodine atom were taken by setting the boxcar gate to different parts of the kinetic energy distribution. The TOF spectra were obtained by setting the pump–probe delay at different fixed positions and averaging the mass spectra over 1500 laser shots with a transient digitizer (10-ns channel resolution).

IV. Results

In Figure 2 the femtosecond transients for the HgI, Hg, and I are shown for parallel polarization of pump (λ_1) and probe (λ_2*) lasers. Time zero for each of these transients is shown with respect to half of the rise time of the HgI_2 parent. The parent mass gives a multiexponential decay which will be discussed in another publication[25] that carefully considers the complete decay (linear and nonlinear behavior) at long times. The measured time shifts, with respect to half the rise of the parent, when monitoring the transition state on different mass fragments are 47 ± 15 fs for HgI, 61 ± 15 fs for I, and 75 ± 15 fs for Hg. (The influence of saturation on the rise time of transients will also be discussed in ref 25.) The time shifts indicate that the initial motion of the wave packet to the transition state from the Franck–Condon region takes ~50 fs. This is consistent with the measured decay on the parent ion signal, as discussed below.

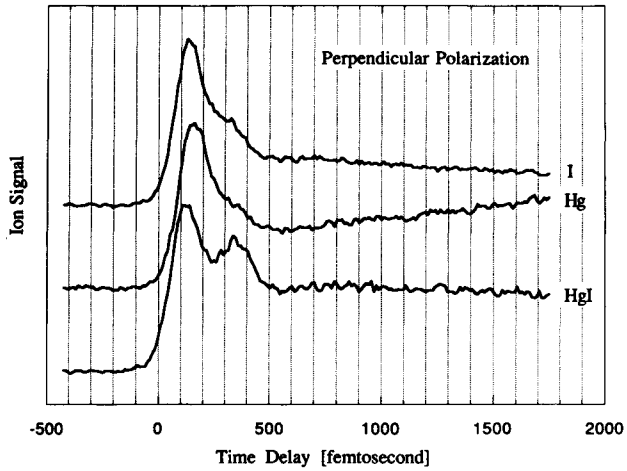

Figure 3. Femtosecond transients obtained by detecting the mass of HgI, Hg, and I for perpendicular polarization. Note the decrease of the second component around 350 fs with respect to the first component, in comparison to parallel laser polarization (Figure 2).

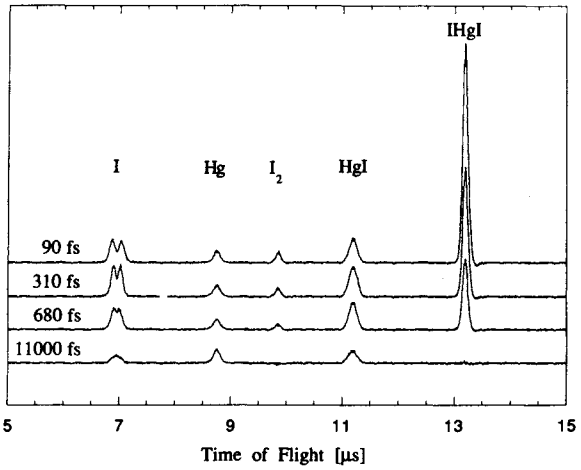

Figure 4. Complete TOF mass spectrum at different time delays, showing the parent IHgI and the nascent fragments.

The transients on all three fragment masses show a double-peak structure within the first 500 fs. We checked the asymptotic behavior of these three transients up to 100 ps: the I transient and HgI transients reach a constant asymptotic value, while the Hg transient increases over several picoseconds. In order to obtain more insight into this behavior discussed in ref 25, we performed careful pump and probe intensity studies on all masses. After 500 fs, the transients in Figure 2 are dominated by multiphoton dynamics. The early time behavior is the one-photon excitation dynamics to the repulsive surface leading to reactions 1 and 2, and our focus here is on these one-photon dynamics to the repulsive continuum (we shall refer to it as the A-continuum). Of particular interest is the early-time behavior of the fragments, their alignment, and their kinetic energy release.

For comparison, in Figure 3 transients on the same masses are shown but now with perpendicular polarization of probe (λ_2*) versus pump (λ_1). Note that the pump polarization for all experiments described here was kept fixed and parallel to the TOF axis. Special care was taken to ensure the same energies in the pump and probe lasers for the two polarizations used. The difference to notice here is that for all transients the second peak structure in the early-time behavior is enhanced for parallel polarization (Figure 2) in comparison to perpendicular polarization (Figure 3).

In Figure 4, TOF spectra are shown for different λ_1–λ_2* delay times: 90 fs is close to the first structure of the transients in Figure 2 and 310 fs is close to the second structure, whereas 680 and 11 000 fs belong to the asymptotic part of the transients. The

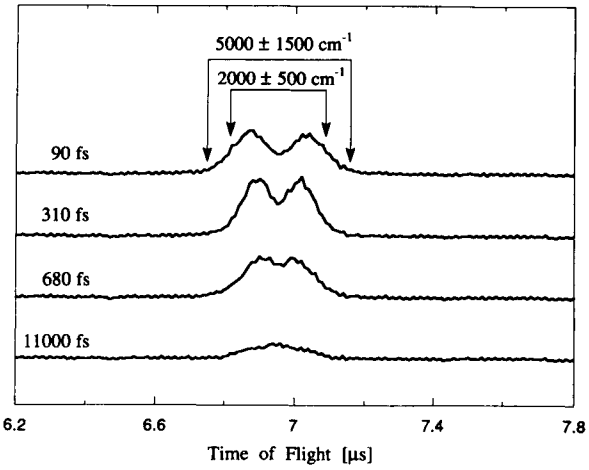

Figure 5. KETOF distribution of I at different time delays. The arrows indicate the kinetic energy release of I associated with the width of the distribution.

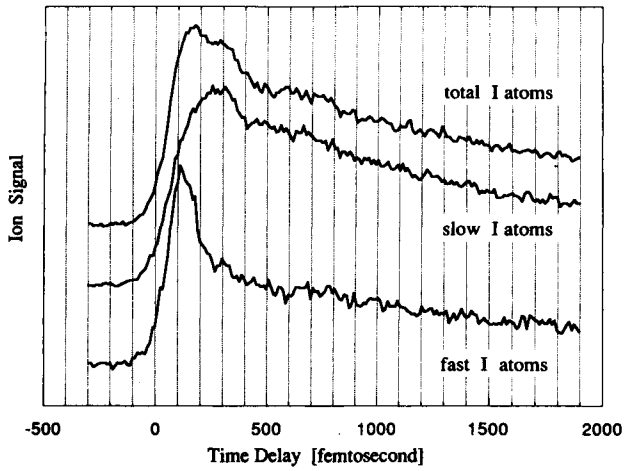

Figure 6. Femtosecond transients detected on the I mass, but with different kinetic energies.

TOF spectra are not normalized; only the time-independent background was subtracted. The decay of the HgI_2 parent and of the I_2 fragment as well as the asymptotic values for the HgI, Hg, and I fragments is clear. An interesting change in the KETOF distribution, with respect to the time delay between pump and probe pulses, is observed on the I fragment.

Figure 5 shows the I portion of Figure 4. In this figure, the TOF spectrum is shown for E = 63 V/cm. The experiment was also performed at other low settings of the electric field to find an average value of the kinetic energy of the I fragment using formula 5. The onset of the KETOF distribution at 90 fs corresponds to a kinetic energy of the I fragment of 5000 ± 1500 cm^{-1}, whereas the 50% value corresponds to 2000 ± 500 cm^{-1}. Formula 7 then gives the total available translational energy (the fragments being I and HgI): using the onset value, it is E_t = 7000 ± 2000 cm^{-1}, while the 50% value yields 2700 ± 700 cm^{-1}.

In order to gain deeper insight into the kinetic energy distribution of I with respect to the pump–probe delay time, transients at different kinetic energies were taken: The transient at the bottom of Figure 6 was recorded with a gate position of our boxcar that monitors only fast fragments with a kinetic energy >2000 cm^{-1} (see Figure 5). We will refer to this transient as the fast I transient. The transient in the middle of Figure 6 was taken by setting the gate to that part of the KETOF distribution that mainly contains energies in the range from 0 to 500 cm^{-1}. Note that such a gate position will also accumulate some of the faster fragments, because only the projection of the dissociation distribution along the TOF axis can be monitored by this technique. This transient is referred to as the slow I transient.

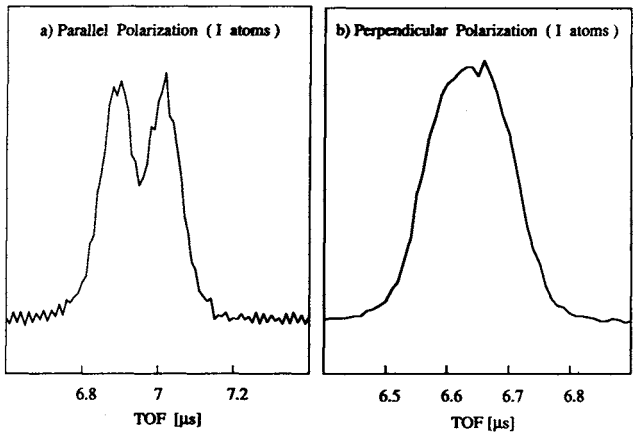

Figure 7. KETOF distribution of I at comparable delay times: (a) parallel laser polarization; (b) perpendicular laser polarization. The difference in flight time is due to different extraction conditions.

The top transient in Figure 6 was obtained by setting the gate to average over the complete KETOF distribution. We will refer to this transient as the total I transient. From the gating experiments, one assigns the first structure in the total I transient to the contribution of the wave packet leading to fast I fragments, whereas the second structure in this transient is due to the wave packet leading to the slow I fragments.

Figure 7 gives an insight into the alignment of the transition moment of the I fragments. In Figure 7a, the KETOF distribution for I is shown at a pump–probe delay time of 310 fs for parallel polarization of the lasers (same as in Figure 6). In Figure 7b, the KETOF spectrum of I for perpendicular polarization is shown at 207-fs delay time. (The difference in flight time is due to different extraction conditions of our TOF spectrometer for these two experiments.) While in the parallel case a splitting in the KETOF distribution is observed, this splitting is not seen in the perpendicular case. This effect is due to the probe laser polarization, since the polarization of the pump was kept parallel to the TOF axis for all the data presented here, as discussed in the following section. (Experiments involving rotation of the pump with respect to the TOF axis are in preparation.)

V. Femtosecond Dynamics and the Reaction Pathway

Figure 8 shows the potential and snapshots of the wave packet for the $[I\cdots Hg\cdots I]^{\ddagger *}$ complex fragmentation along the symmetric and asymmetric stretch coordinates. Parts A and B of Figure 8 correspond to an excitation (310 nm) to 1350 and 8950 cm^{-1}, respectively, above the threshold for total dissociation on surfaces (a) and (b).[2,26] Figure 8A represents the simplest picture of I* channel dissociation with products HgI + I*, I* + HgI, and I* + Hg + I, while Figure 8B represents the simplest picture of I channel dissociation with products HgI + I, I + HgI, and I + Hg + I. The two different excess energies simulate the spin–orbit splitting of 7600 cm^{-1}.

Figure 9 shows the energetics of our λ_1, λ_2* scheme, based on the available spectroscopic information of IHgI and its fragments (see references in figure caption). The 311-nm λ_1 photon initiates the dissociation, whereas the 622-nm probe ionizes either the parent molecule or the transition state in a MPI process. The lowest ionization potential for the parent molecule is 9.5088 ± 0.0022 eV.[27,28] Exciting the ground-state parent molecule, HgI_2, the energy required to produce HgI^+ (+ I + e) is 10.88 ± 0.05 eV,[27,29] and to produce I^+ (+ HgI + e) it is 13.12 ± 0.04 eV.[27,29] The ionization energies of the neutral fragments are 8.23 ± 0.07 eV for HgI,[27] 10.451 eV for I,[30] and 10.437 eV for Hg.[30] If the transition state is probed, it takes at least three probe photons to ionize the parent in a REMPI process, while four probe photons are required to produce HgI^+ and five to yield I^+. On the other hand, five probe photons are needed to ionize the free HgI out

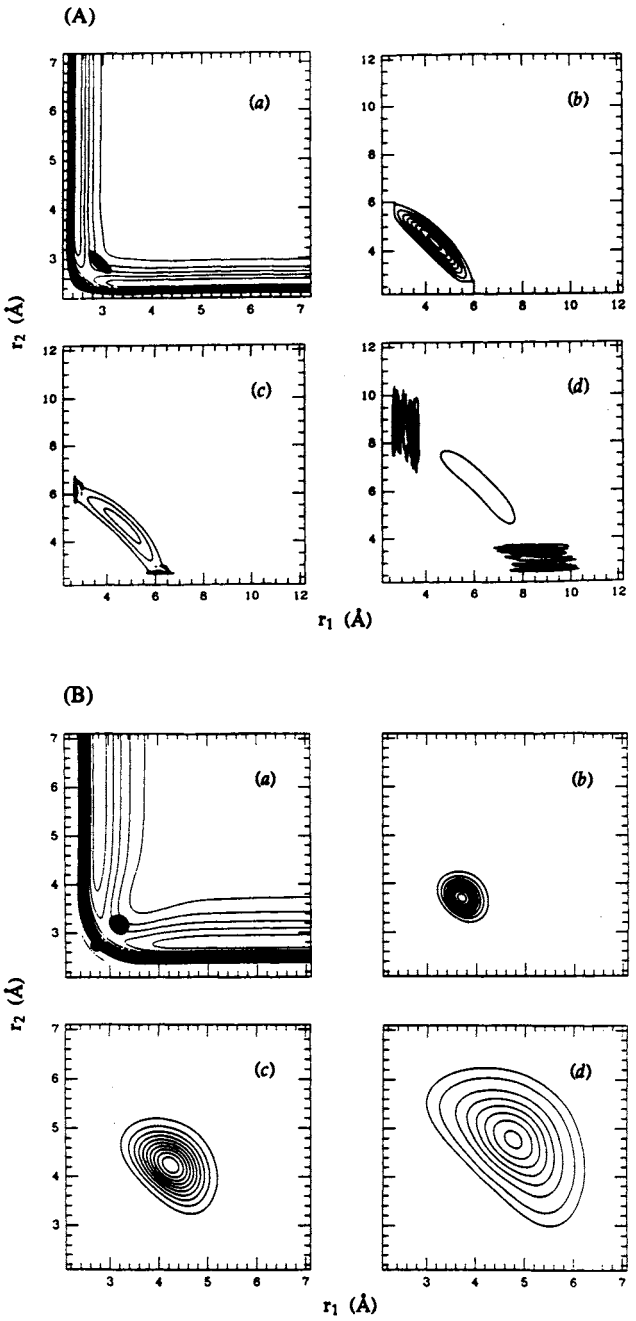

Figure 8. (A) Snapshots of HgI_2 dissociation at 1350 cm^{-1} with respect to total dissociation on surface a.[2,26] This corresponds to I* channel dissociation. The wave packet is shown at different times: (a) 160, (b) 320, (c) 400, (d) 800 fs. (B) The dynamics on surface b at 8950 cm^{-1}, corresponding to I channel dissociation, and at times: (a) 58, (b) 116, (c) 175, (d) 233 fs.

of its ground state in a 1 + 4 REMPI process. Ionizing free $I(^2P_{3/2})$ is a 4 + 2 REMPI process and a 4 + 1 REMPI for free $I^*(^2P_{1/2})$.[30] Free $Hg(^1S_0)$ is also ionized by a 4 + 2 REMPI process.[30] At this wavelength of 622 nm, probing from the transition-state region is consistent with the FTS studies made on this system by LIF detection.[31]

From the energetics, it is clear that reaction channels 1 and 2 are, in principle, open following the creation of the complex. If the complex is bent and/or undergoes bending motion, one additional channel is possible

$$\left[I \overset{Hg}{\diagdown\!\diagup} I \right]^{\ddagger *} \longrightarrow Hg(^1S_0) + I_2 \qquad (8)$$

with molecular iodine elimination. We detect the I_2 mass, but before considering its origin let us examine the potentials.

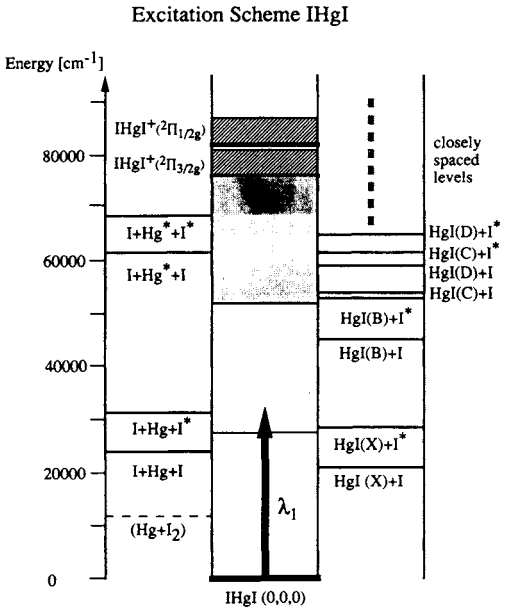

Figure 9. Energetics of the IHgI system. The asymptotic values for symmetric stretch fragmentation and asymmetric stretch fragmentation are shown. Spectroscopic data are taken from ref 30 for the atoms from refs 41 and 77 for IHgI and from refs 41, 78, and 79 for HgI. Ground-state data on IHgI can be found in refs 80 and 81. The lighter shaded excitation area indicates the absorption bands observed by Maya,[77] whereas the darker shaded regions corresponds to higher absorption structures. The excitation wavelength is indicated by λ_1. (I = $^2P_{3/2}$, I* = $^2P_{1/2}$, Hg = $^1S_0$, Hg* = $^3P_0$, HgI(X) = $^2\Sigma^+$, HgI(B) = $^2\Sigma^+$, HgI(C) = $^2\Pi_{1/2}$, HgI(D) = $^2\Pi_{3/2}$).

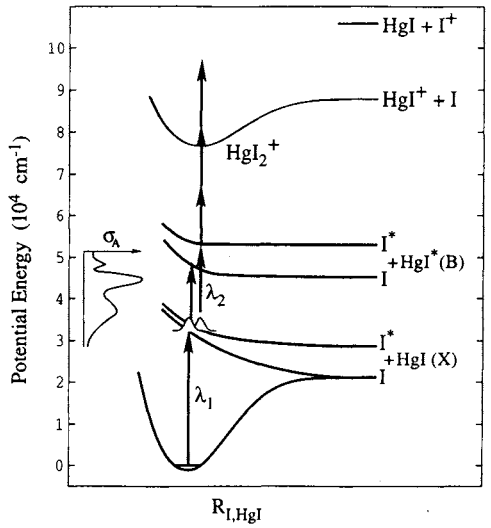

Figure 10. A cut along the asymmetric stretch translational coordinate, together with the absorption cross section,[32] showing the idea for detecting the fragments in the transition state (620 nm) or detecting the free HgI fragments at 390 nm.

The first absorption band of HgI_2 peaks at 265 nm and extends to 350 nm (see Figure 11).[32,33] Leone's group determined the quantum yield of iodine in both spin–orbit states.[32] Production of I*($^2P_{1/2}$) was found to be favored for excitation at wavelengths shorter than 295 nm, while at 310 nm the production of I*($^2P_{1/2}$) is ~20%. Formation of the two spin–orbit states of iodine is assumed to arise from the two potential energy surfaces of HgI_2, which are separately excited at 310 nm (see Figure 10). In the isoelectronic system, CdI_2, the angular distribution of the fragments was measured by Bersohn's group.[34] They found that a perpendicular excitation leads to I($^2P_{3/2}$), whereas the parallel excitation leads to dissociation into the I*($^2P_{1/2}$) frements.

While the ground state of HgI_2 is linear, relativistic *ab initio* calculations on $HgCl_2$ by Wadt[35] predict that the $^1\Sigma_u^+$ state of

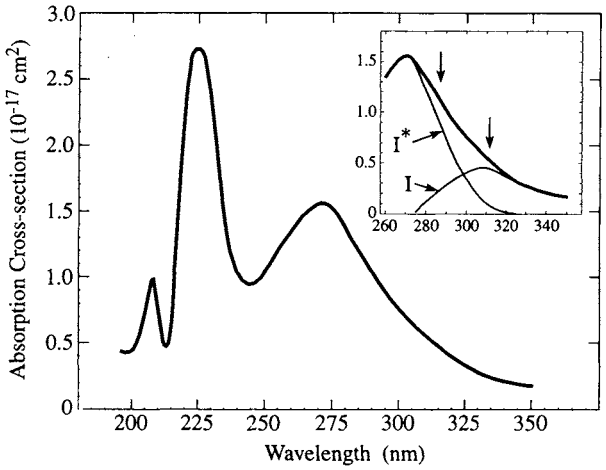

Figure 11. Total absorption cross section for HgI_2.[32] Insert: total HgI_2 absorption cross section and fractional components leading to excited I($5^2P_{1/2}$) and ground state I($5^2P_{3/2}$) atoms upon photodissociation of HgI_2.

this latter molecule is bent by ~80–120°. An analogous nonlinear $^1\Sigma_u^+$ state is expected for HgI_2. Using a simple ligand-to-metal charge-transfer model, including spin–orbit coupling, together with magnetic circular dichroism spectra, Mason[33] concluded that the initial absorption has $\Sigma_u^+(1)$ and Π_u character (total spin–orbit states) with the singlet character $^1\Sigma_u^+$ and $^1\Pi_u$ about 20%, with a linear geometry description. The coupling of bending motion to fragment rotation occurs on a time scale of picoseconds and is therefore relatively insignificant on the time scale of the bond-breaking process near the transition state. This type of rotational dephasing and bending motion has been discussed in detail in refs 1 and 2.

Recent femtosecond studies (using LIF)[2,31] and classical[31] and quantum mechanical calculations[26] from this group revealed the coherent motion from the transition state to final products. This striking type of coherence propagation along the reaction path has now been observed even in solutions[36–38] and examined theoretically[39,40] to determine the forces governing the motion. For our purpose here it is sufficient to connect the LIF findings with those of the MPI-TOF. In the LIF studies, ground-state HgI_2 was excited in a cell by a femtosecond pump pulse at 310 nm. As the HgI molecules from channel 1 separate, they were probed independently by a second femtosecond pulse at either 620 or 390 nm. At short interfragment distances, the separation between the potential energy surfaces of the HgI($X^2\Sigma^+$) state and the HgI($B^2\Sigma^+$) state is smaller than in the asymptotic limit (see Figure 10). Correspondingly, with 620-nm probe, with detection of fluorescence using a monochromator at various detection wavelengths, a double-peak structure was observed and attributed to the slow and fast motions resulting from the two different HgI fragmentation channels 1a. With 390-nm probe, the vibrational product distribution was determined. In the I* channel, relatively little energy is available for vibrational and translational excitation of the HgI X state ($v'' = 7 \pm 1$), whereas in the I channel highly-vibrationally excited HgI X products are formed ($v'' = 29 \pm 2$). Trajectory calculations showed that 60% of the products are formed via process 1b, with Hg + I + I, and 4% via process 1b, with Hg + I + I*.[31] At these energies, the symmetric stretch fragmentation is thus more likely than the asymmetric stretch fragmentation, as is also confirmed by the wave packet calculations.[26]

In the present molecular beam studies, we may deduce the fragmentation energy belonging to the different dissociation channels (see Figures 1 and 12). Taking the spectroscopic data of Wieland[41] for w_e = 125 cm^{-1} and $w_e x_e$ = 1.0 for $v'' \leq 7$ and $w_e x_e$ = 1.5 for $v'' \geq 7$ for the HgI X state, the fragmentation energies can be calculated. The dissociation energy of HgI_2 is 21 000 cm^{-1}.[31] Using formula 7 (*vide supra*) for the transfor-

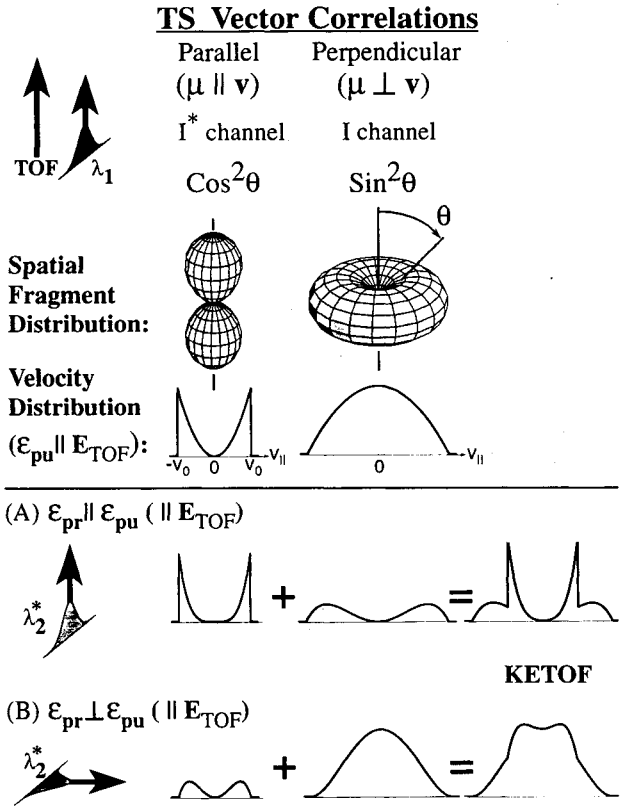

Figure 12. Illustration of the different contributions to our observed KETOF distributions. The top half illustrates the fragment angular distribution and the velocity profiles generated by the pump. The bottom half shows the fragment velocity profiles after probing the transition state. It is assumed that the probing transition moment in the transition state is along the fragmentation direction. The velocity, v, is parallel to the internuclear axis in this case. The complete width of the I channel distribution is greater than that of the I* channel because of the difference in available energy.

mation from total available translational energy to an individual fragment kinetic energy in a collinear two-particle breakup, the kinetic energy of the I atom is calculated and listed below (in the collinear three-particle breakup, the Hg atom will remain at rest):

$$[\text{I}\cdots\text{Hg}\cdots\text{I}]^{\ddagger *} \rightarrow \text{HgI}(X^2\Sigma^+) + \text{I}(^2P_{3/2}) \quad 6400\ \text{cm}^{-1} \quad (9)$$

$$[\text{I}\cdots\text{Hg}\cdots\text{I}^*]^{\ddagger *} \rightarrow \text{HgI}(X^2\Sigma^+) + \text{I}^*(^2P_{1/2}) \quad 2000\ \text{cm}^{-1} \quad (10)$$

$$[\text{I}\cdots\text{Hg}\cdots\text{I}]^{\ddagger *} \rightarrow \text{Hg}(^1S_0) + \text{I}(^2P_{3/2}) + \text{I}(^2P_{3/2}) \quad 4200\ \text{cm}^{-1} \quad (11)$$

$$[\text{I}\cdots\text{Hg}\cdots\text{I}^*]^{\ddagger *} \rightarrow \text{Hg}(^1S_0) + \text{I}(^2P_{3/2}) + \text{I}^*(^2P_{1/2}) \quad 400\ \text{cm}^{-1} \quad (12)$$

We now turn to the different pathways. Before considering the specific cases, we should mention the Hg + I_2 case. If all energy in this fragmentation channel is transformed into translational energy, we would expect a maximum kinetic energy of the I_2 fragment of 9000 cm^{-1}. (The total fragmentation energy is 1.45 eV.[31]) However, we observe only a maximum kinetic energy of 800 cm^{-1} for the I_2 product in the KETOF experiment. As the symmetric stretch fragmentation into the I* channel is only 4% in comparison to 60% for the I channel, we will also exclude this channel in our further considerations. Now we focus on the alignment and the kinetic energy release due to the different primary dissociation processes (channels 9–11).

A. HgI Product Channel. In the one-photon excitation regime, channels 9 and 10 are open to produce HgI via the asymmetric

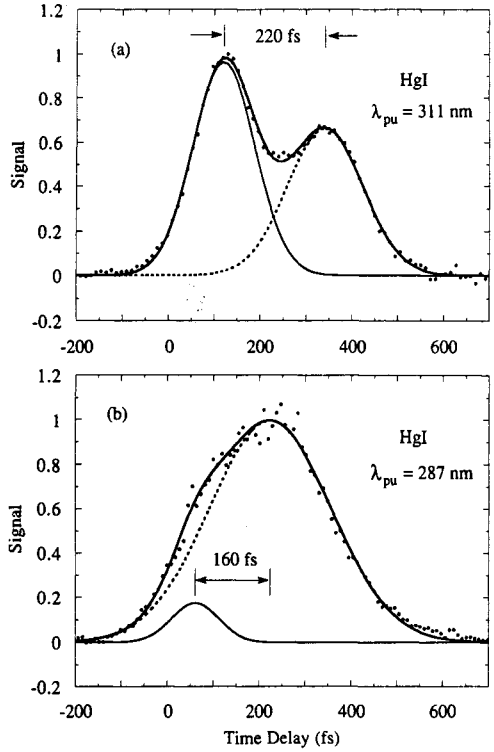

Figure 13. HgI transients for parallel polarization at different pump wavelengths: (a) 311 nm and (b) 287 nm. The long-time component (rise with $\tau \approx 250$ fs; amplitude = 0.46 and 0.042, respectively) convoluted with the Gaussian cross-correlation is removed, leaving the early-time behavior. (a) The first peak (channel 9), at 121 fs, has a fwhm of 159 fs, and its area is 54.4% of the total. The second peak (channel 10), at 341 fs, has a 194 fs fwhm. (b) The peak at 61 fs has a 121 fs fwhm and its area is 6.4%. The peak at 223 fs has a 310 fs fwhm. Deconvoluting the above fwhm widths, F, using the known Gaussian cross-correlation (fwhm $F_c \approx 100$ fs) yields the fwhm values $(F^2 - F_c^2)^{1/2}$.

stretch coordinate. The time shift of half the rise of the HgI transients (Figures 2 and 3) with respect to the half rise time of the parent reflects the time the system needs to enter the transition-state region where the probe photons are resonant with the complex transition, as sketched in Figure 10. The structure and the two peak positions are very similar to that found in the transients obtained in the LIF experiments.[2,31] The first peak is related to channel 9 (high kinetic energy release) whereas the second peak is related to channel 10 (low kinetic energy release). Note that this is not a pure one-dimensional motion, as there is also an oscillatory motion perpendicular to the fragmentation coordinate (Figure 8); this is the motion which leads to coherent excitation in the products.[2,31] In Figure 13a, the HgI transient of Figure 2 is shown, but with the long-time behavior subtracted. Two Gaussians were fitted to the residual, early-time signal. The peaks widths and positions indicate the transient time in the transition state for the two channels (see figure caption, Figure 13).

As the I channel 9 is accessed by a perpendicular transition, the products will predominantly fragment perpendicular to the pump laser polarization. The first probe photon has to make the HgI B ← X ($\Sigma \leftarrow \Sigma$) transition (*i.e.*, a parallel transition). Therefore, the alignment of the HgI transition moment will preferentially be in the plane perpendicular to the pump polarization. If the probe laser polarization is perpendicular to that of the pump, it will lie in this plane. On the other hand, if the probe polarization is parallel to that of the pump, then it will be primarily perpendicular to the HgI transition moment. There is therefore an enhanced REMPI HgI^+ signal of the I channel for perpendicular laser polarization and a reduced REMPI HgI^+ signal for parallel polarization. For the REMPI HgI^+ signal due to the I* channel 10, the argument is reversed as this channel is

accessed by a parallel transition. The HgI transition moment will be preferentially aligned parallel to the pump polarization, and so the probe polarization will be predominantly parallel or perpendicular to this transition moment if it is parallel or perpendicular, respectively, to the pump polarization. This explains the experimental observation that for parallel laser polarization the second component of the HgI transient in Figure 2 is enhanced in comparison to the HgI transient taken with perpendicular polarization, Figure 3. The behavior, also seen in fluorescence,[2] indicates that the excitation process involves a preparation of wave packets on the two different potentials leading to two different fragmentation channels. If the pump were to access only one state, then the system would have to evolve through a conical intersection in order to release I and I*, and a distinct polarization dependence would not be expected.

B. I Product Channel. Atomic iodine can be produced in this one-photon excitation regime along the symmetric stretch coordinate (channel 11) or via the asymmetric stretch coordinate (channels 9 and 10). In Figure 5 it is shown that the onset of the kinetic energy distribution contains I fragments with kinetic energies of about 5000 ± 1500 cm^{-1}. As the I channel 9 is accessed by a perpendicular transition and the pump laser is parallel to the TOF axis, a broad I distribution is expected for this dissociation channel, where the onset of the distribution should reflect the kinetic energy release of the process as described above. The parallel transition leading to the I* channel 10 should deliver a double structure in the kinetic energy distribution. The 50% value of this double structure in Figure 5 corresponds to 2000 ± 500 cm^{-1}. Both values are in reasonable agreement with the calculated values given above (see Appendix).

Assuming the 5p orbital (singly occupied) of I is aligned along the fragmentation axis in an asymptotic limit, and therefore gives rise to a parallel type transition in the REMPI probing of the transition state, a similar behavior with respect to pump–probe laser polarization is expected for the I transients: enhanced I^+ REMPI signal from the I* channel for parallel probing and reduced I^+ REMPI signal from the same channel for perpendicular probing. This behavior is most obvious in the two KETOF spectra of Figure 7 where the KETOF distribution for parallel pump–probe laser polarization shows the splitting for the I* channel, whereas for perpendicular laser polarization the distribution is the broad one. The latter is typical of a perpendicular pump transition when the pump laser polarization is parallel to the TOF axis, as explained above and in the Appendix and also illustrated in Figure 12 (assuming direct collinear fragmentation and negligible influence of molecular rotation justified by the short time scale we observe the two different distributions). According to the trajectory calculations, 60% of the complexes fragment along the symmetric stretch coordinate, leading to calculated kinetic energies of $\sim$4200 cm^{-1}. We conclude that this dissociation pathway is also accessed by the perpendicular pump transition. (We would have expected a double structure in the KETOF distribution resembling the 4200-cm^{-1} splitting if this fragmentation would be induced by a parallel type transition.) As the REMPI probing of I* need not necessarily occur at the same internuclear distance as the HgI REMPI probing (in the transition-state region), and as there is a contribution to the I fragments from the dissociation along the symmetric stretch coordinate, the double-peak structure in the I transient (Figure 2) is not as pronounced as in the HgI transients.

The final proof that the double structure is due to iodine atoms coming from different dissociation channels is demonstrated in Figure 6. The fast iodine atoms from the asymmetric stretch fragmentation along the HgI + I coordinate and from the symmetric stretch fragmentation contribute mainly to the first peak of the total transient, whereas the second peak is due to the slow iodine atoms originating from a fragmentation along the HgI + I* coordinate. It is therefore concluded that at these internuclear separations of the transition state (within $\sim$50-fs motion) the two potentials (I and I*) are well-defined, and there is not enough mixing to scramble the identity of the anisotropy.

C. Hg Product Channel. According to the one-photon excitation regime, Hg product comes from the dissociation along the symmetric stretch coordinate. The time shift of this transient is again related to the time the system needs to evolve into the transition-state region. In the Hg transient of Figure 2 there is also a double structure seen in the early-time behavior. This double structure is not attributed to a dynamical resonance as a strong polarization dependence is observed. Note that the symmetric motion is bound for low-excitation energies (see Figure 8), and at moderate energies above dissociation partial reflection of the wave packet is possible. The second peak in the Hg transient is suppressed for perpendicular laser polarization and enhanced for parallel laser polarization (Figures 2 and 3). We therefore suggest that the second peak in the Hg transient is due to the HgI + I* dissociation monitored through the fragmentation of HgI^+ to Hg^+ and I. As discussed above, the HgI^+ REMPI signal is enhanced for parallel laser polarization and decreased for perpendicular laser polarization. The observation that the second peak in the Hg transient has nearly the same position as the second peak in the HgI transient (Figure 2) supports this explanation.

D. Effect of Total Energy Change. Results were also obtained at $\lambda_1 = 287$ nm and $\lambda_2^* = 622$ nm. A typical transient on HgI for parallel laser polarization is shown in Figure 13b. The low-amplitude, long-time component has been suppressed (see figure caption). The double-peak structure, seen clearly at $\lambda_1 = 311$ nm (Figure 2 and Figure 13a), is not as conspicuous here. At 311 nm the first peak (channel 9) constitutes 54.4% of the signal, while the second peak (channel 10) contributes 45.6%. In contrast, at 287-nm excitation the first peak (I channel) accounted for only 6.4%. The transient is time-shifted by about 80 fs with respect to the time zero of the parent. The fwhm of the second peak alone is 310 fs and that of the whole transient is 330 fs, much broader than the cross-correlation. The I and the Hg transients do not show a double-peak structure at this pump wavelength, but they too are time-shifted with respect to the parent transient. KETOF transients on "fast" and "slow" I fragments were similar, to within statistical error, to the total transient obtained detecting I fragments at all velocities along the TOF axis.

These results are in agreement with the separation of the I and I* potentials at short times and in accord with the yield ratios at long times (ref 32 and Figure 11). At 311-nm excitation, $\sim$20% of the total iodine atom yield is in the form of I*, while at 287 nm about 80% of the total iodine atom yield is in its spin–orbit excited state (ignoring the small thermal energy difference: in ref 32 a cell at 453 K was used, while here the sample was at 445 K, followed by an expansion through the nozzle with no backing pressure). As discussed above, the yield of HgI originating from the I* channel is enhanced for parallel λ_2^* laser polarization. Thus, the double structure due to the different fragmentation channels should be dominated by the I* channel peak at high (287-nm) excitation energy. It is interesting to note, from the molecular dynamics simulations (see Figure 8 and refs 2 and 26), that at higher energies the packet spreads more and faster into the symmetric stretch coordinate, but the leaking into the asymmetric coordinate becomes slower.

VI. Conclusions

This contribution develops femtosecond kinetic energy time-of-flight (KETOF) as a method of probing the vectorial dynamics of transition states. Studies of the $[I\cdots Hg\cdots I]^{\ddagger *}$ transition-state complex in a molecular beam are reported and used to illustrate the approach. The reaction was initiated by a femtosecond laser pulse at 311 nm (or 287 nm) and followed by a time-delayed

probe laser (622 nm) that ionizes the complex and the fragments in a TOF mass spectrometer. This REMPI ionization enabled us to follow the initial dynamics of the wave packet along the symmetric and asymmetric coordinates, resolving the early, less than 50-fs motions. The time for the system to enter the transition state was obtained by measuring time delays in the rise time of the fragments in comparison to the rise of the parent molecule. The transient time of the complex in the transition state ranges from 120 to 300 fs, depending on the available energy. Product fragment masses (Hg, I, HgI) are also studied.

Different dissociation channels yielding the same fragment mass (I) were resolved in two ways: by the nature of the parent transition moment and by the kinetic energy release to the fragment. The channels giving rise to HgI + I and I + Hg + I were both accessed via a perpendicular transition and due to the high kinetic energy release they yielded fast atomic iodine fragments. However, the HgI + I* channel, having less translational energy available, produces slow iodine fragments. This channel is accessed via a parallel transition. The femtosecond resolution of the fragment anisotropy identifies the alignment of the transition moment with respect to fragmentation. As the spectrometer axis is well-defined, rotating the pump and probe laser polarization with respect to the TOF axis gives insight into the vectorial properties, but now during the transition state.

The approach, outlined in Figure 12, promises applications in relation to vector correlations of the dynamics, with the addition of the time resolution to probe early internuclear separations. The same concept should be extended to bimolecular reactions and to other detection schemes.[2,12,13,15,16,18,20] Improvement in time-of-flight resolution can also be made using pulsed acceleration TOF mass spectrometry.[42] There are theoretical and experimental extensions of this work. Theoretically, the treatment of correlations and anisotropy during the transition state needs improvement: in the course of angular momentum evolution maybe a hindered rotation picture would be appropriate. On the experimental side, we plan further experiments aimed at resolving the photoelectrons, using ZEKE,[19] and this should help us map out the kinetic energy change with time.

Acknowledgment. This work was supported by a grant from the Air Force Office of Scientific Research and by the National Science Foundation.

Appendix: Anisotropy and Rotational Alignment in Pump-Probe Experiments

When a molecule is excited by a pump laser, the optical transition dipole moment, μ, is preferentially aligned along the pump polarization direction, ϵ_{pu}. If the parent subsequently dissociates, then the resulting fragments will be characterized by their velocity, v, and angular momentum, J. Because of the alignment of the parent transition moment (μ), the fragments will be described by a recoil anisotropy (μ–v correlation[43–49]) and will have a rotational alignment (μ–J correlation[10,50–53]). In addition to v and J of the fragment being correlated with μ of the parent, they must also be correlated with each other.[54–60] The theory for the angular distributions and correlations has been developed thoroughly (see the excellent review by Hall and Houston[8]). Both LIF (Doppler profiles; see refs 8–10 and 60–63) and MPI detection (see refs 8–10 and 64–70) have been used to measure the correlations and to extract information such as the nature of the parent transition and an estimate of the lifetime of the dissociating parent molecule.

Relevant to the approach presented here, we shall consider the μ–v correlations first, followed by the effect of REMPI probing with detection along a TOF axis. All correlations will be incorporated in order to examine the velocity profile and the time scales. The consequences of probing in the transition-state region are also considered.

1. Angular Distribution Created by the Pump Pulse. For an electric dipole transition in which a single photon excites a parent molecule the transition probability is expressed by

$$P \propto |\epsilon_{pu} \cdot \mu|^2 \tag{A1}$$

where ϵ_{pu} is the pump polarization direction and μ is the transition dipole moment of the parent molecule ($\mu = \mu_{fi} = \langle f|\mu|i\rangle$). Hence, if γ is the angle between ϵ_{pu} and μ, then the normalized transition probability is

$$P = \frac{3}{4\pi}\cos^2\gamma = \frac{1}{4\pi}[1 + 2P_2(\cos\gamma)] \tag{A2}$$

where $P_2(x) = {}^1/_2(3x^2 - 1)$ is the second-degree Legendre polynomial. This relationship, expressed as $P(\theta)$, the angular recoil velocity distribution, may in general be written as

$$P(\theta) = \frac{1}{4\pi}[1 + \beta P_2(\cos\theta)] \tag{A3a}$$

where θ is the angle between the final recoil velocity, v, and the pump polarization vector, ϵ_{pu}, and β is the anisotropy parameter (μ–v correlation).[43–48]

In certain experiments, the "axis of detection", e.g. TOF axis, is well-defined in the laboratory. If the pump pulse is parallel to this axis (see Figure 16) and the fragments can be detected along this axis, then eq A3a can be expressed in terms of the projection of the fragment velocity parallel to this axis, $v_\parallel$:

$$P(v_\parallel) = \frac{1}{2v_0}\left[1 + \beta P_2\left(\frac{v_\parallel}{v_0}\right)\right] \tag{A3b}$$

which is a parabola or "inverted parabola" depending on the value of β (see section 2B of this appendix and Figure 15). For LIF detection, an equation of the same parabolic form is obtained.[60] Let us now consider first the effect of no rotation and next take rotational effects into account.

A. No Rotational Effects (of the Parent). If the molecule dissociates instantaneously on absorption of the light and if the kinetic energy of dissociation is very large compared to the rotational energy of the molecule, then β is given simply by

$$\beta = 2P_2(\cos\chi_0) \tag{A4}$$

where χ_0 is a fixed angle between the parent transition moment, μ, and the direction of dissociation (given by the final recoil velocity, v, for negligible rotation).[44,46] For a diatomic molecule the direction of dissociation is the internuclear axis and thus $\chi_0 = 0°$ or 90°. For a polyatomic molecule χ is less restricted. It can be generalized to describe an arbitrary recoil distribution $P(\chi)$[47]

$$\beta = 2\int_0^\pi P_2(\cos\chi)P(\chi)\,d\chi \tag{A5}$$

The anisotropy parameter, being the average of $P_2(\cos\chi)$ over the probability distribution of χ, must lie between the maximum and minimum values of $P_2(\cos\chi)$, *i.e.*, $-1 \le \beta \le 2$.

Let us return to the case of $P(\chi) = \delta(\chi - \chi_0)$ and consider three cases. If the excitation involves a parallel transition moment ($\mu \| v$), then $\chi_0 = 0, \beta = 2$, and $P(\theta) = (3/4\pi)\cos^2\theta$, *i.e.*, a dumbbell-shaped angular distribution with respect to the ϵ_{pu} direction. In this case, the fragment is most likely to travel along (collinear or anticollinear) the direction of ϵ_{pu} (Figure 12). On the other hand, with a perpendicular transition moment ($\chi_0 = 90°$), we obtain $\beta = -1$ and $P(\theta) = (3/8\pi)\sin^2\theta$, a toroidal probability distribution with respect to the ϵ_{pu} direction (Figure 12). In this case, the fragment has maximum probability to travel at right angles to ϵ_{pu}. In the very unlikely case that χ_0 happens to be 54.7° ($\beta = 0$), we would obtain an isotropic distribution: $P(\theta) = 1/4\pi$.

B. Effects of Rotation. If the parent molecule rotates with angular velocity ω there are two rotational effects to be considered,

even for a diatomic molecule, both of which reduce the magnitude of β. First, if the excited molecule lives for an average lifetime, T_0, before dissociating, then[45,48]

$$\beta = 2P_2(\cos\chi_0)\frac{1+(\omega T_0)^2}{1+4(\omega T_0)^2} \tag{A6}$$

where the probability that the molecule has not dissociated in a time t is given by the distribution

$$P(t) = \frac{1}{T_0}\exp\left[-\frac{t}{T_0}\right] \tag{A7}$$

Second, when the molecule finally does dissociate, the nascent fragments will have a tangential velocity due to the rotation of the molecule in addition to the radial velocity of recoil. This effect is significant if the rotational energy of the molecule is not negligible compared to the kinetic energy release in the fragmentation. The effect has been treated for a diatomic molecule, yielding[47]

$$\beta = 2P_2(\cos\chi_0)\left\{\frac{P_2(\cos\alpha)+(\omega T_0)^2-3(\omega T_0)\sin\alpha\cos\alpha}{1+4(\omega T_0)^2}\right\} \tag{A8a}$$

$$\tan\alpha = v_t/v_0 \tag{A8b}$$

where α is the angle between the asymptotic recoil velocity, v, and v_0, the fragment radial recoil velocity. This tangential velocity effect has also been treated separately from the finite lifetime effect. For a small rotation angle, α, the effect is to reduce β, given by (A6), by a factor of[45,48]

$$1 - {}^3/_2\sqrt{2}kT/E_{rel} + O((kT/E_{rel})^2) \tag{A9}$$

where E_{rel} is the energy of relative motion of the fragments. This is compatible with the more general expression (A8) of Busch and Wilson:[47] the tangential velocity effect (if considered as (A8a) with $\omega T_0 = 0$) reduces the magnitude of β by $P_2(\cos\alpha)$. For small α, $\alpha \approx \omega r/v_0$ and $P_2(\cos\alpha) = 1 - (3/2)\,(w^2r^2/v^2)$, where r is the distance from the CM to the fragment. The two approaches then agree in the limit of small α because $\omega^2r^2/v^2 \propto \langle E_{rot}\rangle/E_{rel} \propto kT/E_{rel}$.

2. Probing to Ionization with KETOF Detection. *A. Free Fragment Probing.* When the probe pulse arrives (at time delay, t_D, after the pump), it sees an anisotropic fragment angular recoil distribution, characterized by β. Unlike the pump, the probe also encounters an anisotropic rotational distribution. Here first we consider the anisotropies for free fragment probing ($t_D \gg T_0$).

In general,[59] the intensity of any optical process acting on a set of rotating molecules, characterized by its moments or multipoles, ${}^{(R)}A_Q^K$, is given by

$$I = \sum_{K,Q} q_Q^K\,{}^{(R)}A_Q^K \tag{A10}$$

where the q_Q^K coefficients depend on the physics of the optical process, $R(Ox,Oy,Oz)$ is a fixed axis system, and K and Q are integers with $-K \le Q \le K$.[70] For REMPI detection details of the rotational selection rules for the ionization step are needed.[71] This difficulty is removed if the last step is a very high probability (near 1) isotropic ionization step (saturation), in which case the anisotropy of the whole process only depends on the preceding steps made by the probe.

In a typical experiment, a projection of the velocities along the TOF axis is detected, giving rise to a velocity profile. The following conditions are considered: (i) The linear pump polarization, ϵ_{pu}, lies along an Oz axis. (ii) Dissociation leads to a final single fragment recoil speed, v_0. (iii) The linear probe polarization, ϵ_{pr}, lies along an Oz' axis, and the probing process exhibits rotational

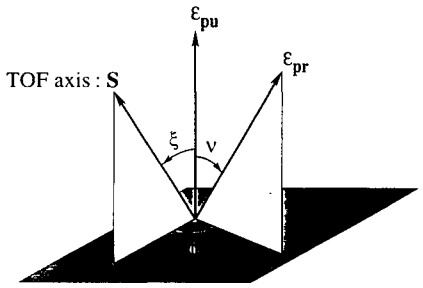

Figure 14. Definition of the angles (θ,ν,ϕ), characterizing the relative arrangement of the vectors $(\epsilon_{pu},\epsilon_{pr},S)$ involved in the REMPI KETOF method.

and inversion invariance with respect to this axis. The q_2 coefficients (see later) of this REMPI process are assumed known. (iv) The velocity profiles of the ionized fragments are detected along an Oz'' axis (TOF axis) in this REMPI TOF method.

The ${}^{(R)}A_Q^K$ moments in (A10) must be expressed explicitly in terms of the velocity component $v_\parallel$ along the TOF axis to obtain the velocity profile, $g(v_\parallel)$, of the ionized fragment ($g(v_\parallel)$ is used in ref 70, and here we use $P(v_\parallel)$). Mons and Dimicoli[70] used the procedure reported by Dixon[60] to arrive at the appropriate expressions. The moments are expressed in terms of the bipolar moments, $b_Q^K(k_1,k_2)$, containing all the angular information of the system: the μ–v–J correlations; k_1 and k_2 are respectively the orders at which translational and rotational motions are involved. The velocity profile contains not only $P_0(x)$ and $P_2(x)$ like the neutral fragment profile (A3) but also terms in $P_4(x)$ and $P_6(x)$, where $x = v_\parallel/v_0$. However, the high-order Legendre polynomial contributions are difficult to evidence experimentally. According to Mons and Dimicoli, if, in addition, no strong angular correlations are expected, it seems reasonable to neglect these higher-order terms and to focus on the first coefficients: β, A, C, and C'. Here $\beta = 2b_0^2(2,0)$ is the previously encountered μ–v anisotropy parameter of eq A3, $A = A_0^2(J) = {}^4/_5 b_0^2(0,2)$ is the alignment parameter,[50,54,70,72,73] $C = \sqrt{5}b_0^0(2,2)$ is the first-order v–J correlation coefficient, and $C' = \sqrt{7}/_2 b_0^2(2,2)$ is the first μ–v–J correlation coefficient. Under these assumptions, the experimental velocity profiles can be expressed in the form[70]

$$g(v_\parallel) \propto 1 + \beta_{eff}P_2(v_\parallel/v_0) \tag{A11a}$$

where β_{eff} is an effective anisotropy, and the equation has now similarity to the pump-alone case (A3). The β_{eff} parameter is defined by

$$\beta_{eff} = g_2/g_0 \tag{A11b}$$

with

$$g_0 = 1 + q_2AP_2(\cos\nu) \tag{A12a}$$

and

$$g_2 = \beta P_2(\cos\xi) + q_2C\{2P_2(\cos\xi)P_2(\cos\nu) + 6\cos\xi\sin\xi\sin\nu\cos\nu\cos\phi + {}^3/_2\sin^2\xi\sin^2\nu\cos2\phi\} - {}^2/_7 q_2C\{4P_2(\cos\xi)P_2(\cos\nu) + 6\cos\xi\sin\xi\sin\nu\cos\nu\cos\phi - 3\sin^2\xi\sin^2\nu\cos2\phi\} \tag{A12b}$$

in which ξ is the angle between the pump polarization direction, ϵ_{pu}, and the TOF axis, S, and ν is the angle between ϵ_{pu} and ϵ_{pr}. The angle ϕ is the angle between the plane containing ϵ_{pu} and S and the plane containing ϵ_{pu} and ϵ_{pr} (see Figure 14). The real coefficient q_2[54,72,74–76] specifies the probed quantum state, and its dynamical range is typically $[-{}^1/_2, {}^1/_2]$.[54] The second-degree Legendre polynomial, $P_2(v_\parallel/v_0) = (3(v_\parallel/v_0)^2 - 1)/2$, in (A11a), expresses the fact that the velocity profile is parabolic, where $v_\parallel$ lies in the range $-v_0 \le v_\parallel \le v_0$. The limits $v_\parallel = \pm v_0$ describe fragments whose final recoil velocity is aligned either collinear

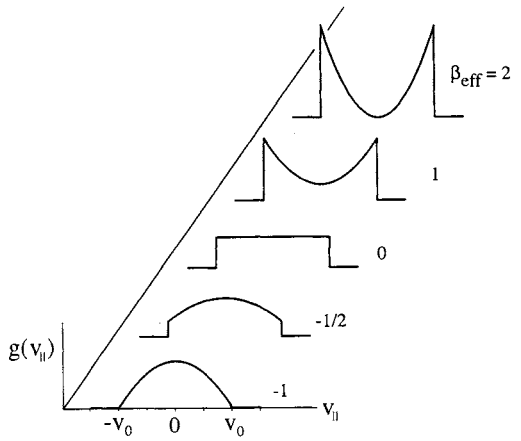

Figure 15. Velocity profiles of monokinetic fragments, detected in a REMPI KETOF experiment. Fragmentation is induced by the linearly polarized pump pulse, ϵ_{pu}, generating well-defined μ–v–J correlations, described by β, A, C, and C'. The linearly polarized probe pulse (ϵ_{pr}) induces a REMPI process on the well-defined rovibronic state(s) of the fragments, characterized by the q_2 coefficient. The effective anisotropy parameter, $\beta_{eff} = \beta_{eff}(\beta,A,C,C',q_2,...)$, describes the velocity profiles. See eq A11.

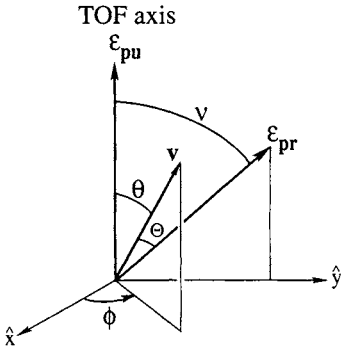

Figure 16. Experimental axis system used: the pump polarization is along the TOF axis, and the probe polarization is at an angle ν to the pump. The direction of recoil is given by the velocity, v.

or anticollinear with the TOF axis. The point $v_\parallel = 0$ corresponds to fragments whose final recoil velocity is perpendicular to the TOF axis. The velocity profile is shown in Figure 15 for different values of β_{eff}. Mons and Dimicoli[70] considered some specific pump–probe geometries. Note that if the pump and probe lasers propagate collinearly and the TOF axis is perpendicular to this propagation direction, then $\phi = 0°$ or 180°.

B. Probing the Transition-State Region. In the following section we consider the case when the packet motion is on the femtosecond time scale so that any rotational effects may be neglected both before and after probing. We shall consider the case in which the probe arrives at a short time delay, t_D, after the pump and finds the excited complex in the transition-state region ($t_D \leq T_0$). Let us assume that the probing transition moment, μ_2, is aligned along the recoil velocity, $v(t)$. This velocity is unaltered by the probing, but its magnitude may change in the subsequent evolution of the probed complex leading to two free fragments (one of which is the ion detected). Hence the probe transition is parallel.

Following the pump excitation, the probability of finding the complex with a recoiling velocity $v(\theta,\phi)$ in a solid angle $d\Omega$ (=sin $\theta\, d\theta\, d\phi$) is given by (A3)

$$P(\theta)\, d\Omega = (1/4\pi)[1 + \beta P_2(\cos\theta)]\, d\Omega \qquad (A13)$$

where θ is the angle between v and ϵ_{pu} (Figure 16), and β is given by (A4) or (A5). The probability of probing one of the excited complexes is given by

$$P_{pr}(\Theta) \propto \cos^2\Theta \qquad (A14)$$

where Θ is the angle between $v(\theta,\phi)$ and ϵ_{pr}. The probability of finding a probed molecule in the direction given by $v(\theta,\phi)$ is then given by

$$P(\theta,\phi)\, d\Omega \propto [1 + \beta P_2(\cos\theta)]\cos^2\Theta\, d\Omega \qquad (A15)$$

In general, the velocity profile along the TOF axis involves an integration around this axis, adding up the probability that an ion is traveling with a velocity whose projection along the TOF axis is $v_\parallel$ (an analogous treatment, but for free fragments and expressing the distribution as a function of a Doppler shift, can be found in the Appendix of ref 60). For simplicity, we present the case in which the pump polarization, ϵ_{pu}, is along the TOF axis (see Figure 16). Using $v_\parallel = v_0 \cos\theta$, it follows that

$$P(v_\parallel)\, dv_\parallel \propto [\int_{\theta\,\text{fixed}} P(\theta,\phi)\, d\phi]\, dv \qquad (A16)$$

in which $-v_0 \leq v_\parallel \leq v_0$. Making use of the identity

$$\cos\Theta = \sin\theta \sin\phi \sin\nu + \cos\theta \cos\nu \qquad (A17)$$

and carrying out the integration yields

$$P(v_\parallel)\, dv_\parallel \propto \left[1 + \beta P_2\left(\frac{v_\parallel}{v_0}\right)\right]\left[1 + 2P_2(\cos\nu)P_2\left(\frac{v_\parallel}{v_0}\right)\right] dv_\parallel \qquad (A18)$$

where ν is the angle between ϵ_{pu} and ϵ_{pr}, and the TOF axis is along ϵ_{pu}. Equation A18 describes the velocity profile obtained in a process involving one pump photon and one probe transition from the transition state. (If additional steps are made by the probe, then (A14) must be altered.)

If the neutral fragments following pump excitation could be detected, then the observed velocity profile would be given by $1 + \beta P_2(v_\parallel/v_0)$. The effect of probing the transition state is to introduce the second factor, $1 + 2P_2(\cos\nu)P_2(v_\parallel/v_0)$, in (A18). If the polarization of the probe is oriented at the magic angle to that of the pump ($\nu = 54.7°$), then this second factor reduces to unity and the velocity profile is unaltered by the probing.

Let us consider the two distinct cases of a parallel ($\beta = 2$) and a perpendicular pump transition ($\beta = -1$) and in each case investigate the effect of probing with a polarization that is either parallel or perpendicular to the pump polarization. These cases are illustrated in Figure 12.

(i) Parallel pump transition: $\beta = 2$. The velocity profile generated by the pump *only* is proportional to $(v_\parallel/v_0)^2$, *i.e.*, parabolic and peaking at $\pm v_0$. Probing the transition state alters this profile in a way that depends on the orientation of the probe polarization:

(a) TOF$\parallel$pump$\parallel$probe ($\nu = 0°$). In this case, the resulting velocity profile is given by

$$P(v_\parallel) \propto (v_\parallel/v_0)^2(v_\parallel/v_0)^2 = (v_\parallel/v_0)^4 \qquad (A19)$$

The velocity profile is thus enhanced and sharpened near the limits $\pm v_0$.

(b) TOF$\parallel$pump$\perp$probe ($\nu = 90°$).

$$P(v_\parallel) \propto (v_\parallel/v_0)^2\,[1 - (v_\parallel/v_0)^2] \qquad (A20)$$

The velocity profile is greatly altered and the yield of ions is less than case (a) above.

(ii) Perpendicular pump transition: $\beta = -1$. The velocity profile generated by the pump only is proportional to $1 - (v_\parallel/v_0)^2$, *i.e.*, parabolic and peaking at $v_\parallel = 0$, corresponding to a preference for fragmentation in the plane perpendicular to the pump polarization. This profile is also altered upon probing the transition state.

(a) TOF‖pump‖probe ($\nu = 0°$). The resulting velocity profile here is given by

$$P(v_\parallel) \propto [1 - (v_\parallel/v_0)^2](v_\parallel/v_0)^2 \qquad \text{(A21)}$$

The velocity profile is thus changed and the yield is lower than for case (b) below.

(b) TOF‖pump⊥probe ($\nu = 90°$).

$$P(v_\parallel) \propto [1 - (v_\parallel/v_0)^2][1 - (v_\parallel/v_0)^2] = [1 - (v_\parallel/v_0)^2]^2 \qquad \text{(A22)}$$

The velocity profile is enhanced about $v_\parallel = 0$ due to the probing.

3. Kinetic Energy Release. The velocity profile detected in a KETOF experiment is that of the ion fragments. The width, Δt, of this profile determines the kinetic energy of the ion (see eq 5). These ions may be produced either by probing the neutral fragments or by probing the transition state.

A. Free Fragment Probing. If the internuclear separation is sufficiently large (no potential energy between fragments) that the nascent fragment has acquired its final recoil speed, v_0, then, upon probing to ionization, its velocity will not be altered due to conservation of momentum. Of the translationally available excess energy after probing, the ejected electron carries away a fraction $(1 + m_e/m_{ion})^{-1}$, which is almost unity, leaving the fragment velocity essentially unchanged. Therefore, the fragment velocity is not changed upon probing, and this holds true independent of the excess energy to which the neutral fragment is probed, *i.e.*, independent of the probe wavelength; the electron always carries the excess translational energy of recoil, even if the ion has internal energy. The kinetic energy of the ion (see eq 7) is then governed by the total available translational energy, E_t, in the CM frame after the pump excitation. If we define the ground state of the parent as the zero of potential energy, then if the pump accesses the potential energy surface $V_1(R)$, the available energy (eq 6) may be written

$$E_{avl} = V_1(R_{pu}) - V_1(\infty) = E_{int} + E_t \qquad \text{(A23)}$$

where $V_1(R_{pu}) = E_{int}^P + h\nu_{pu}$, and $V_1(\infty) = D_0^0$.

B. Probing the Transition-State Region. On the other hand, if the pump–probe delay time is small enough ($t_D \leq T_0$) that the transition state is probed, then the picture is different. In the transition state, the available energy, partitioned among internal and translational degrees of freedom, is given by

$$E_{avl}^{TS}(R) = V_1(R_{pu}) - V_1(R) = E_{int}(R) + E_t(R) \qquad \text{(A24)}$$

If the same number of probe photons enter in the probe excitation, then the same total energy will be available to the entire system. However, when the transition state is probed to a dissociative state above the ionization level, the energy excess above the asymptotic level (free ion and free fragment) can be shared by the two nascent parts as well as by the ejected electron. The kinetic energy of the resulting ion thus depends on the probe wavelength or excess energy probed to. Immediately after probing, the velocity, $v(t)$, is unchanged. However, the subsequent evolution is on a new potential energy surface, $V_2(R)$, with a different total available energy. If the kinetic energy, E_e, of the photoelectron is measured, then the difference potential may be determined. It should be noted that if the potential energy, V_1, is dropped significantly, then the ionization process is characteristic of the asymptotic limit (see the discussion in section 3A) and the kinetic energy release is similar to that of the neutrals on V_1. As mentioned in the text, this feature will be utilized in future experiments.

References and Notes

(1) Dantus, M.; Bowman, R. M.; Baskin, J. S.; Zewail, A. H. *Chem. Phys. Lett.* **1989**, *159*, 406.

(2) Zewail, A. H. *Faraday Discuss. Chem. Soc.* **1991**, *91*, 207; *J. Chem. Soc., Faraday Trans. 2* **1989**, *85*, 1221 and references therein.

(3) Felker, P. M.; Zewail, A. H. *J. Chem. Phys.* **1987**, *86*, 2460. Baskin, J. S.; Felker, P. M.; Zewail, A. H. *J. Chem. Phys.* **1987**, *86*, 2483.

(4) Felker, P. M. *J. Phys. Chem.* **1992**, *96*, 7844 and references therein.

(5) Heather, R.; Metiu, H. *Chem. Phys. Lett.* **1989**, *157*, 505.

(6) Benjamin, I.; Wilson, K. R. *J. Chem. Phys.* **1989**, *90*, 4176.

(7) Waldeck, J. R.; Shapiro, M.; Bersohn, R. *J. Chem. Phys.*, to be published.

(8) Hall, G. E.; Houston, P. L. *Annu. Rev. Phys. Chem.* **1989**, *40*, 375.

(9) Riley, S. J.; Wilson, K. R. *Faraday Discuss. Chem. Soc.* **1972**, *53*, 132. Bersohn, R. In *Advances in Gas-Phase Photochemistry and Kinetics*; Ashfold, M. N. R., Baggott, J. E., Eds.; Royal Society of Chemistry: London, 1987; p 1. Wodtke, A. M.; Lee, Y. T. *Ibid*, p 31. Docker, M. P.; Hodgson, A.; Simons, J. P. *Ibid*, p 115. Ashfold, M. N. R.; Lambert, I. R.; Mordaunt, D. H.; Morley, G. P.; Western, C. M. *J. Phys. Chem.* **1992**, *96*, 2938.

(10) Simons, J. P. *J. Phys. Chem.* **1984**, *88*, 1287.

(11) Schlag, E. W.; Neusser, H. *J. Acc. Chem. Res.* **1983**, *16*, 355.

(12) Baumert, T.; Buehler, B.; Grosser, M.; Thalweiser, R.; Weiss, V.; Wiedenmann, E.; Gerber, G. *J. Phys. Chem.* **1991**, *95*, 8103.

(13) Dantus, M.; Janssen, M. H. M.; Zewail, A. H. *Chem. Phys. Lett.* **1991**, *181*, 281. Janssen, M. H. M.; Dantus, M.; Guo, H.; Zewail, A. H. *Chem. Phys. Lett.*, in press.

(14) Baumert, T.; Herek, J. L.; Zewail, A. H. *J. Chem. Phys.*, in press.

(15) Baumert, T.; Thalweiser, R.; Gerber, G. *Chem. Phys. Lett.* **1993**, *209*, 29. Baumert, T.; Roettgermann, C.; Rothenfusser, C.; Thalweiser, R.; Weiss, V.; Gerber, G. *Phys. Rev. Lett.* **1992**, *69*, 1512.

(16) Wei, S.; Purnell, J.; Buzza, S. A.; Stanley, R. J.; Castleman, A. W., Jr. *J. Chem. Phys.* **1992**, *97*, 9480.

(17) Baumert, T.; Buehler, B.; Thalweiser, R.; Gerber, G. *Phys. Rev. Lett.* **1990**, *64*, 734.

(18) Walkup, R. E.; Misewich, J. E.; Glownia, J. H.; Sorokin, P. P. *J. Chem. Phys.* **1991**, *94*, 3389. Glownia, J.; Misewich, J.; Walkup, R.; Kaschke, M. *T. Appl. Phys.* **1992**, *70*, 3.

(19) Mueller-Dethlefs, K.; Sander, M.; Schlag, E. W. *Z. Naturforsch.* **1984**, *39A*, 1089. Mueller-Dethlefs, K.; Sander, M.; Schlag, E. W. *Annu. Rev. Phys. Chem.* **1991**, *42*, 109.

(20) Chen, Y.; Hunziker, L.; Ludowise, P.; Morgen, M. *J. Chem. Phys.* **1992**, *97*, 2149.

(21) Wiley, W. C.; McLaren, I. H. *Rev. Sci. Instrum.* **1955**, *26*, 1150. In this article the energy resolution was discussed and related to the initial fragment kinetic energy.

(22) Ling, J. H.; Wilson, K. R. *J. Chem. Phys.* **1975**, *63*, 101.

(23) Rosker, M. J.; Dantus, M.; Zewail, A. H. *J. Chem. Phys.* **1988**, *89*, 6113.

(24) Bowman, R. M.; Dantus, M.; Zewail, A. H. *Chem. Phys. Lett.* **1989**, *161*, 297. Herek, J. L.; Pedersen, S.; Bañares, L.; Zewail, A. H. *J. Chem. Phys.* **1992**, *97*, 9046.

(25) Pedersen, S.; Baumert, T.; Zewail, A. H. *J. Phys. Chem.*, following paper in this issue.

(26) Gruebele, M.; Roberts, G.; Zewail, A. H. *Philos. Trans R. Soc. London, A* **1990**, *332*, 223.

(27) Linn, S. H.; Tzeng, W.-B.; Brom, J. M., Jr.; Ng, C. Y. *J. Chem. Phys.* **1983**, *78*, 50.

(28) Eland, J. H. D. *Int. J. Mass Spectrom. Ion Phys.* **1970**, *4*, 37.

(29) Rosenstock, J. *Phys. Chem. Ref. Data* **1977**, *6*, 1, 677.

(30) Moore, C. E. *Atomic Energy Levels*; Circular 467; Natl. Bur. Stand.: Washington, DC, 1958; Vol. III.

(31) Dantus, M.; Bowman, R. M.; Gruebele, M.; Zewail, A. H. *J. Chem. Phys.* **1989**, *91*, 7437. Bowman, R. M.; Dantus, M.; Zewail, A. H. *Chem. Phys. Lett.* **1989**, *156*, 131.

(32) Hofmann, H.; Leone, S. R. *J. Chem. Phys.* **1978**, *69*, 3819.

(33) Savas, M. M.; Mason, W. R. *Inorg. Chem.* **1988**, *27*, 658.

(34) Kawasaki, K.; Lee, S. J.; Bersohn, R. *J. Chem. Phys.* **1979**, *71*, 1235.

(35) Wadt, W. R. *J. Chem. Phys.* **1980**, *72*, 2469.

(36) Benjamin, I.; Banin, U.; Ruhman, S. *J. Chem. Phys.* **1993**, *98*, 8337. Banin, U.; Ruhman, S. *J. Chem. Phys.* **1993**, *98*, 4391.

(37) Scherer, N. F.; Ziegler, L. D.; Fleming, G. R. *J. Chem. Phys.* **1992**, *96*, 5544.

(38) Observation of coherent dissociation in solutions of HgI_2 has been made recently: Hochstrasser, R. M. Private communication.

(39) Manz, J.; Reischl, B.; Schroeder, T.; Seyl, F.; Warmuth, B. *Chem. Phys. Lett.* **1992**, *198*, 483.

(40) Ben-Nun, M.; Levine, R. D. *Chem. Phys. Lett.* **1993**, *203*, 450.

(41) Wieland, K. *Z. Elektrochem.* **1960**, *64*, 761.

(42) Hwang, H. J.; El-Sayed, M. A. *Chem. Phys. Lett.* **1990**, *170*, 161; *J. Chem. Phys.* **1991**, *94*, 4877; *J. Phys. Chem.* **1991**, *95*, 8044; *J. Chem. Phys.* **1992**, *96*, 856; *J. Phys. Chem.* **1992**, *96*, 8728. See also: Loo, R. O.; Hall, G. E.; Haerri, H.-P.; Houston, P. L. *J. Phys. Chem.* **1988**, *92*, 5.

(43) Zare, R. N.; Herschbach, D. R. *Proc. IEEE* **1963**, *51*, 173.

(44) Bersohn, R.; Lin, S. H. *Ad. Chem. Phys.* **1967**, *16*, 67.

(45) Jonah, C. *J. Chem. Phys.* **1971**, *55*, 1915.

(46) Zare, R. N. *Mol. Photochem.* **1972**, *4*, 1.

(47) Busch, G. E.; Wilson, K. R. *J. Chem. Phys.* **1972**, *56*, 3638.

(48) Yang, S.; Bersohn, R. *J. Chem. Phys.* **1974**, *61*, 4400.

(49) Scmiedl, R.; Dugan, H.; Meier, W.; Welge, K. H. *Z. Phys. A.* **1982**, *304*, 137.

(50) Greene, C. H.; Zare, R. N. *J. Chem. Phys.* **1983**, *78*, 6741.

(51) Greene, C. H.; Zare, R. N. *Annu. Rev. Phys. Chem.* **1982**, *33*, 119. See also: Fano, U.; Macek, J. H. *Rev. Mod. Phys.* **1973**, *45*, 553 and ref 62.

(52) Chamberlain, G. A.; Simons, J. P. *J. Chem. Soc., Faraday Trans. 2* **1975**, *71*, 2043.

(53) Chamberlain, G. A.; Simons, J. P. *Chem. Phys. Lett.* **1975**, *32*, 355.
(54) Dubs, M.; Bruehlmann, U.; Huber, J. R. *J. Chem. Phys.* **1986**, *84*, 3106.
(55) Hall, G. E.; Sivakumar, N.; Houston, P. L. *Phys. Rev. Lett.* **1986**, *56*, 1671. Hall, G. E.; Sivakumar, N.; Chawla, D.; Houston, P. L.; Burak, I. *J. Chem. Phys.* **1988**, *88*, 3682.
(56) Docker, M. P.; Hodgson, A.; Simons, J. P. *Chem. Phys. Lett.* **1986**, *128*, 264.
(57) Gericke, K.-H.; Klee, S.; Comes, F. J.; Dixon, R. N. *J. Chem. Phys.* **1986**, *85*, 4463.
(58) Grunewald, A. U.; Gericke, K.-H.; Comes, F. J. *Chem. Phys. Lett.* **1987**, *133*, 501.
(59) Case, C. A.; McClelland, G. M.; Herschbach, D. R. *Mol. Phys.* **1978**, *35*, 541.
(60) Dixon, R. N. *J. Chem. Phys.* **1986**, *85*, 1866.
(61) Nadler, I.; Mahgerefteh, D.; Reisler, H.; Wittig, C. *J. Chem. Phys.* **1985**, *82*, 3885.
(62) Vasudev, R.; Zare, R. N.; Dixon, R. N. *J. Chem. Phys.* **1984**, *80*, 4863.
(63) Bain, A. J.; McCaffery, A. J. *J. Chem. Phys.* **1984**, *80*, 5883; **1985**, *83*, 2627, 2632, 2641.
(64) Mons, M.; Dimicoli, I. *Chem. Phys. Lett.* **1986**, *131*, 298.
(65) Hall, G. E.; Sivakumar, N.; Ogorzalek, R.; Chawla, G.; Haerri, H.-P.; Houston, P. L. *Faraday Discuss. Chem. Soc.* **1986**, *82*, 13.
(66) Black, J. F.; Powis, I. *Chem. Phys.* **1988**, *125*, 375.
(67) Loo, R. O.; Hall, G. E.; Haerri, H.-P.; Houston, P. L. *J. Phys. Chem.* **1988**, *92*, 5.
(68) Kawasaki, M.; Sato, H.; Fukuroda, A.; Kikuchi, T.; Kobayashi, S.; Arikawa, T. *J. Chem. Phys.* **1987**, *86*, 4431.
(69) Krautwald, H. J.; Schneider, L.; Welge, K. H.; Ashfold, M. N. R. *Faraday Discuss. Chem. Soc.* **1986**, *82*, 99.
(70) Mons, M.; Dimicoli, I. *J. Chem. Phys.* **1989**, *90*, 4037.
(71) Jacobs, D. C.; Zare, R. N. *J. Chem. Phys.* **1986**, *85*, 5457.
(72) Kummel, A. C.; Sitz, G. O.; Zare, R. N. *J. Chem. Phys.* **1988**, *88*, 7357.
(73) See also ref 1.
(74) Bain, A. J.; McCafferty, A. J. *J. Chem. Phys.* **1985**, *85*, 2627.
(75) Kummel, A. C.; Sitz, G. O.; Zare, R. N. *J. Chem. Phys.* **1986**, *85*, 6874.
(76) Kummel, A. C.; Sitz, G. O.; Zare, R. N. *J. Chem. Phys.* **1988**, *88*, 6707.
(77) Maya, J. *J. Chem. Phys.* **1977**, *67*, 4976.
(78) *Gmelins Handbuch der anorganischen Chemie, Quecksilber, Teil B – Lieferung 2*; Verlag Chemie GmbH: Weinheim, 1967; p 34.
(79) Jordan, K. J.; Lipson, R. H.; Yang, D. S. *J. Chem. Phys.* **1992**, *97*, 9099.
(80) Loewenschuss, A.; Ron, A.; Schnepf, O. *J. Chem. Phys.* **1969**, *50*, 2502.
(81) Bernstein, R. B. *Chemical Dynamics via Molecular Beam and Laser Techniques*; Oxford University Press: Oxford, 1982.